

# Systematic study of the relationship between nuclear structure and reactions for the $^{10}\text{Be}$ nucleus

T. Furumoto<sup>1,\*</sup>, T. Suhara<sup>2</sup>, and N. Itagaki<sup>3,4</sup>

<sup>1</sup>*College of Education, Yokohama National University, Yokohama 240-8501, Japan*

<sup>2</sup>*Matsue College of Technology, Matsue 690-8518, Japan*

<sup>3</sup>*Department of Physics, Osaka Metropolitan University, Osaka, 558-8585, Japan*

<sup>4</sup>*Nambu Yoichiro Institute of Theoretical and Experimental Physics (NITEP), Osaka Metropolitan University, Osaka 558-8585, Japan*

\*E-mail: [furumoto-takenori-py@ynu.ac.jp](mailto:furumoto-takenori-py@ynu.ac.jp)

Received April 21, 2023; Revised May 29, 2023; Accepted May 29, 2023; Published May 31, 2023

.....  
We systematically investigate the relationship between the nuclear structure and reaction in the  $^{10}\text{Be}$  nucleus using a theoretical framework. The structure of the  $^{10}\text{Be}$  nucleus is constructed with a cluster model based on a microscopic viewpoint. In this paper, the  $^{10}\text{Be}$  nucleus is prepared with different structures by manipulating the parameters of an effective nucleon–nucleon interaction. The nuclear structure and expectation values of physical quantities are drastically changed by the modification. We summarize such changes and show the effects on the elastic and inelastic scatterings for proton and  $^{12}\text{C}$  targets in the microscopic coupled-channel calculation. Of especial interest, we recently reported the visualization of the dineutron correlation in  $^{10}\text{Be}$  on proton inelastic scattering in [Phys. Rev. C **104**, 034613 (2021)]. In this preceding work, we found that changing the degree of dineutron correlation in  $^{10}\text{Be}$  leads to drastic changes of the inelastic cross section for the  $2_2^+$  state. The development (or breaking) of the dineutron correlation is governed by the strength of the spin–orbit interaction of the structure calculation. However, in the previous work, some of the realistic physical points were missing, for example, the binding energy (BE). Therefore, we reconstruct the  $^{10}\text{Be}$  nucleus by adjusting the effective nucleon–nucleon interaction to obtain a reasonable BE of the ground state. With this improvement, we again discuss the dineutron correlation in the  $^{10}\text{Be}$  nucleus. We reconfirm the way to measure the degree of development (or breaking) of the dineutron cluster structure: its sensitivity to the inelastic cross section of the  $2_2^+$  state of  $^{10}\text{Be}$ . Subject Index cluster model, folding model, dineutron correlation, effective nucleon–nucleon interaction.  
.....

Subject Index D06, D12, D13, D27

## 1. Introduction

For decades, the microscopic description based on the nucleon–nucleon ( $NN$ ) interaction for the nuclear structure and reaction has been developed. These microscopic approaches are successful in describing and understanding the properties of the nuclear structure and reaction quite well. Although the  $NN$  interaction has been investigated since the discovery of the proton and neutron, its behavior is still not fully understood, especially in the nuclear medium. Therefore, in these microscopic structure and reaction calculations, the effective  $NN$  interaction with parameters has often been used. There are many microscopic models based on the (effective)  $NN$  interaction for the nuclear structure [1–14]. The microscopic description has led to the understanding of a great deal of nuclear structure information. Recently, improvements

in computational technology have made it possible to perform even more precise nuclear structure calculations. Most microscopic approaches to nuclear reactions are based on the folding model. This has been developed for the nucleon and heavy-ion scatterings [15–31]. It is remarkable that the recent microscopic description of the nuclear structure and reaction is based on the realistic  $NN$  interaction.

Through these analyses, enhancing the connection between the microscopic nuclear structure and reaction models has been attempted. By the connection, microscopic nuclear reaction calculations accurately incorporating nuclear structure information were performed, and many experimental data were successfully reproduced [32–37]. In addition, this approach to the microscopic nuclear structure and reaction gives interesting predictions [30,38–40]. In such approaches, density is one of the key intermediaries because it is one of the inputs in the microscopic folding model and one of the outputs in the microscopic nuclear structure model. The diagonal and transition densities contain a large amount of nuclear structure information. The microscopic folding model tells us the nuclear structure information in the observable through the density. Therefore, to derive the diagonal and transition densities not only microscopically but also macroscopically is important to connect nuclear structure and reaction. Here, we note that it is possible to observe the structure information in experimental data if the diagonal and transition densities have a sensitivity to the nuclear structure. Therefore, it is important to make the relationship among density, nuclear structure, reaction mechanism, and observable clearer.

Here, we demonstrate an example of how changing the nuclear structure in an artificial way affects the reaction. The change is closely related to the development and breaking of the dineutron correlation as reported in Ref. [41], where we discussed the dineutron correlation and its breaking because of the spin–orbit interaction. The persistence of the dineutron cluster is sensitive to the choice of the strength of the spin–orbit interaction in the structure calculation, even if the binding energy (BE) of the neutrons from the threshold is kept constant. Although the dineutron structure is favored when the spin–orbit interaction is weak, the spin–orbit interaction with realistic strength significantly breaks the dineutron structure. In Ref. [40], we found that the inelastic cross section of the  $2_2^+$  state is drastically dependent on the development and breaking of the dineutron correlation. With the advancement of microscopic approaches, such a reliable and interesting analysis is now feasible. This is because the ground ( $0_1^+$ ) and  $2_2^+$  states belong to the  $K = 0$  and  $K = 2$  rotational bands, respectively, and the transition between them is suppressed when the two valence neutrons perform independent particle motion around the core with the two  $\alpha$  structure. However, forming the dineutron configuration breaks the axial symmetry and allows the inter-band transition. Here the spin–orbit interaction is the essential factor.

In this study, we perform systematic calculations to reveal the relation between the nuclear structure and reaction of the  $^{10}\text{Be}$  nucleus. The present  $^{10}\text{Be}$  nucleus is constructed under the assumption of the four-body ( $\alpha + \alpha + n + n$ ) cluster model. The stochastic multi-configuration mixing method enables the description of many exotic cluster structures [42,43]. We focus on the low-lying ( $0_1^+$ ,  $2_1^+$ , and  $2_2^+$ ) states. In the microscopic cluster model, we modify the various parameters for the effective  $NN$  interaction. The energies, nuclear size, and expectation values of  $\langle \mathbf{L} \cdot \mathbf{S} \rangle$  (one-body operator) and  $\langle \mathbf{S}^2 \rangle$  (two-body operator) are calculated to investigate the dependence of the parameters for the  $NN$  interaction. The transition strengths with multipolarity  $\lambda = 2$  are listed for the proton, neutron, isoscalar (IS), and isovector (IV) parts, respectively. The diagonal and transition densities are also calculated. The densities are applied

to the microscopic coupled channel (MCC) calculation. With the MCC model, we calculate  $^{10}\text{Be}$  elastic and inelastic scatterings by proton and  $^{12}\text{C}$  targets at  $E/A = 59.4$  and  $200$  MeV. The present model well reproduces the experimental data up to backward angles. In addition, we provide the inelastic cross section of the  $2_2^+$  state. The effect of the change of the parameters in the microscopic structure calculation is discussed on the elastic and inelastic scattering cross sections derived from the MCC calculation. In addition, we reconstruct the  $^{10}\text{Be}$  nucleus by adjusting the BE, which was ignored in the previous systematic calculation. With this improvement, we again discuss the possibility of observing the degree of development and breaking of the dineutron correlation in  $^{10}\text{Be}$  through the  $2_2^+$  inelastic cross section.

This paper is organized as follows. In Sect. 2, we briefly introduce the present structure and reaction models. In Sect. 3, we list the results of the microscopic cluster model with the modified parameters. We also show the results of the elastic and inelastic cross sections with the modified nuclear structure information. We will discuss the effect of the value of the parameters in the nuclear structure calculation. In addition, we show the results of the reconstructed  $^{10}\text{Be}$  nucleus by reproducing the BE by simultaneously adjusting the spin-orbit strength and the Majorana parameter. The development and breaking of the dineutron correlation in  $^{10}\text{Be}$  are again discussed. Lastly, we summarize this paper in Sect. 4.

## 2. Formalism

We first construct the  $^{10}\text{Be}$  nucleus within the 4-body ( $\alpha + \alpha + n + n$ ) cluster model. With the diagonal and transition densities obtained from the microscopic cluster calculation, the  $^{10}\text{Be} + p$  and  $^{10}\text{Be} + ^{12}\text{C}$  elastic and inelastic scatterings are given by the MCC calculation in the same manners as in Refs. [39,40]. To avoid repetition, we mainly give additional points in this section. The details of the structure and reaction calculations are provided in Refs. [39,40,44,45].

### 2.1. Microscopic cluster model

The  $^{10}\text{Be}$  nucleus is constructed by the stochastic multi-configuration mixing method based on the microscopic cluster model [42,43]. The calculation method is almost the same as in Ref. [40].

The additional calculation in this paper is as follows. For the Hamiltonian, the two-body interaction includes the central, spin-orbit, and Coulomb parts. The Volkov No.2 effective potential is applied to the central part [46] as,

$$V^{(\text{central})}(r) = (W - MP^\sigma P^\tau + BP^\sigma - HP^\tau) \times (V_1 \exp(-r^2/c_1^2) + V_2 \exp(-r^2/c_2^2)), \quad (1)$$

where  $c_1 = 1.01$  fm,  $c_2 = 1.8$  fm,  $V_1 = 61.14$  MeV,  $V_2 = -60.65$  MeV, and  $W = 1 - M$ . Here, we often use the parameter setting as  $M = 0.60$  and  $B = H = 0.08$  [39,40,44], which reproduces the  $\alpha$ - $\alpha$  scattering phase shift. Meanwhile, different values for the parameters  $M$  and  $B = H$  are employed in the investigations of various nuclei [10,47–49]. Therefore, we examine in the range of 0.52, 0.54, 0.56, 0.58, 0.60, 0.62, and 0.64 for  $M$  in this paper. We also investigate the effect of  $B = H$  in the range of 0–0.20. However, the effect is minor in the calculated results. Therefore, we omit to show the results of  $B = H$  in this paper. In addition, we again introduce the spin-orbit term of the G3RS potential [50,51],

$$V^{(\text{spin-orbit})}(r) = V_{\text{LS}}(e^{-d_1 r^2} - e^{-d_2 r^2})P^3 O \mathbf{L} \cdot \mathbf{S}, \quad (2)$$

where  $d_1 = 5.0 \text{ fm}^{-2}$  and  $d_2 = 2.778 \text{ fm}^{-2}$ . The operator  $\mathbf{L}$  represents the relative angular momentum, and  $\mathbf{S}$  represents the spin ( $\mathbf{S}_1 + \mathbf{S}_2$ ).  $P(^3O)$  is the projection operator onto the triplet odd state. As in Ref. [40], the strength of the spin-orbit interaction,  $V_{\text{LS}}$ , is also treated as a parameter in this paper. This value is often fixed around 2000 MeV to reproduce the data of the  $^{10}\text{Be}$  nucleus. In this paper, we show the results with  $V_{\text{LS}} = 0, 500, 1000, 1500,$  and  $2000$  MeV to compare the development and breaking of the dineutron correlation while the effect was investigated in the range of  $V_{\text{LS}} = 0\text{--}4000$  MeV in Ref. [40]. In addition, we give an additional calculation which is simultaneously adjusted for the  $V_{\text{LS}}$  and  $M$  parameters to reproduce the BE of the ground state in this paper.

To connect the nuclear structure and reaction calculations, we prepare the diagonal and transition densities in the same manner as in Ref. [5].

## 2.2. MCC model

Next, we introduce the MCC model based on the MPa interaction [52,53]. The present MCC model has been successful in reproducing and predicting experimental data [31,36,45,54]. The detailed MCC calculation procedure for the folding potential is described in Refs. [28,40,45,55]. Then, we briefly introduce the single- and double-folding model calculations.

The single-folding model potential is simply described as

$$U_{\alpha \rightarrow \beta}^{(SF)}(R; E/A) = \int \rho_{I_\alpha \rightarrow I_\beta}(r) v(s, \rho; E/A) dr, \quad (3)$$

where  $R$  is the radial distance between the incident  $^{10}\text{Be}$  nucleus and the target proton.  $\alpha$  and  $\beta$  mean the channel number of the initial and final states, respectively.  $I_\alpha$  and  $I_\beta$  are spins of the initial and final states, respectively.  $E/A$  is the incident energy per nucleon.  $\rho_{I_\alpha \rightarrow I_\beta}$  is the diagonal ( $\alpha = \beta$ ) and transition ( $\alpha \neq \beta$ ) densities;  $s$  is the radial distance between a nucleon in the projectile nucleus and the target proton, and  $s = r - R$ . We note that the description of Eq. (3) is simplified; in the actual calculation, the proton and neutron densities are separately folded with the proton-proton and proton-neutron interactions, respectively. The Coulomb potential is also obtained by folding the  $NN$  Coulomb interaction and proton density. The knock-on exchange part and the spin-orbit part are obtained in the same manner as in Refs. [40,45].

The double-folding model potential is also provided, as

$$U_{\alpha \rightarrow \beta}^{(DF)}(R; E/A) = \int \rho_{I_\alpha \rightarrow I_\beta}(\mathbf{r}) \rho'_{I'_\alpha \rightarrow I'_\beta}(\mathbf{r}') v(s, \rho; E/A) d\mathbf{r} d\mathbf{r}', \quad (4)$$

where  $I'_\alpha$  and  $I'_\beta$  are the spins of the initial and final states for the target nucleus, respectively.  $\rho'_{I'_\alpha \rightarrow I'_\beta}$  is the diagonal ( $\alpha = \beta$ ) and transition ( $\alpha \neq \beta$ ) densities for the target nucleus. Here,  $s = r - r' - R$ . The frozen density approximation is applied to  $\rho$  in  $v$ . The frozen density approximation is the standard prescription to describe the nucleus-nucleus system and its efficiency is verified in Refs. [29,31]. The knock-on exchange part is obtained in the same manner as in Refs. [38,39].

When the single- and double-folding potentials are applied to the nuclear reaction, we often modify the strength of the imaginary part of the potential to reproduce the data. We apply the incident-energy-dependent renormalization factor,  $N_W = 0.5 + (E/A)/1000$  [54], for the imaginary part in this paper. We note that no additional parameter is needed to calculate the  $^{10}\text{Be}$  scatterings by the proton and  $^{12}\text{C}$  targets.

### 3. Results

The calculated results will be introduced and discussed in this section. We first show the dependence on the parameters ( $V_{LS}$  and  $M$ ) for the BE, radius, and expectation values of  $\langle \mathbf{L} \cdot \mathbf{S} \rangle$  and  $\langle \mathbf{S}^2 \rangle$  of the  $0_1^+$ ,  $2_1^+$ , and  $2_2^+$  states, respectively. Here,  $\langle \mathbf{L} \cdot \mathbf{S} \rangle$  is the expectation value of the one-body operator and the sum of the spin-orbit operator of the nucleons, whereas  $\langle \mathbf{S}^2 \rangle$  is the two-body operator, which is the square of the sum of the one-body spin operator over the nucleons. In the investigation of the dependence on the parameters ( $V_{LS}$  and  $M$ ), we regard the standard values of  $V_{LS} = 2000$  MeV,  $M = 0.60$ , and  $B = H = 0.08$  as references. The quadrupole transition strength between each state is also introduced. In addition, we discuss the effect of change in the nuclear structure on the elastic and inelastic cross sections.

When we calculate the  $^{10}\text{Be} + ^{12}\text{C}$  system, we apply the  $^{12}\text{C}$  density obtained by  $3\alpha$ -RGM [3] to the MCC calculation. The  $0_1^+$ ,  $2_1^+$ , and  $0_2^+$  states of the  $^{12}\text{C}$  nucleus are included because the excitation states are well known to have a strong channel coupling effect. In this paper, all combinations of the spin states of each of the incident and target particles are incorporated into the coupled-channel calculations.

After that, we discuss the relation between the dineutron correlation and the inelastic cross section at the realistic physical point. Concretely, we show additional results in which the  $M$  and  $V_{LS}$  parameters are simultaneously adjusted without changing the BE of the ground state as in Ref. [41]. In order to evaluate the effect of the dineutron correlation on the structure and reaction, we prepare the pure dineutron basis and compare it with a more realistic one.

#### 3.1. Systematic calculation with microscopic cluster model

Here we show the dependence of the structure on the parameters ( $V_{LS}$  and  $M$ ). The parameters give various BEs, radii, and expectation values of  $\langle \mathbf{L} \cdot \mathbf{S} \rangle$  and  $\langle \mathbf{S}^2 \rangle$  for the  $0_1^+$ ,  $2_1^+$ , and  $2_2^+$  states. This systematic analysis clarifies the role of each parameter ( $V_{LS}$  and  $M$ ) in  $^{10}\text{Be}$ . In addition, the quadrupole transition strengths between each state are examined. The transition strengths are also changed together with the property of the nuclear structure. We will discuss the effect of the property of the nuclear structure on the elastic and inelastic cross sections.

3.1.1. *Dependence on  $V_{LS}$ .* Here, we show the obtained nuclear structure and reaction's dependence on  $V_{LS}$  in the Hamiltonian of the nuclear structure calculation. The results are essentially the same as in Ref. [40]. However, we show the calculation results as a table instead of a figure to discuss the  $^{10}\text{Be}$  structure in this paper.

Table 1 shows many calculated results. However, we already discussed the detail of the calculated BEs; root mean squared radii for the point proton ( $r_p$ ), point neutron ( $r_n$ ), and point nucleon matter ( $r_m$ ); the expectation values of  $\langle \mathbf{L} \cdot \mathbf{S} \rangle$  and  $\langle \mathbf{S}^2 \rangle$  for the neutron; and the quadrupole transition strengths of  $B(\text{E}2)$  and the neutron part  $B((\text{E}2)_n)$  in Ref. [40]. From another perspective, we see IS and IV transition strengths. The obtained IS transition strengths from  $2_1^+$  to  $0_1^+$  stay in the range of 30–60 fm<sup>4</sup>. The IV transition strengths from  $2_1^+$  to  $0_1^+$  get gradually smaller as  $V_{LS}$  grows. On the other hand, the IS transition strengths from  $2_2^+$  to  $0_1^+$  are drastically changed by the  $V_{LS}$  value. This effect on the cross section will be discussed later. Here, we also discuss the transition strength from the  $2_2^+$  state to the  $2_1^+$  state. The  $B(\text{E}2; 2_2^+ \rightarrow 2_1^+)$  value becomes smaller when the strength of the  $V_{LS}$  value becomes larger. In Ref. [41], it is mentioned that the increase of the  $B(\text{E}2; 2_2^+ \rightarrow 2_1^+)$  value with the decrease of the  $V_{LS}$  value

**Table 1.** BE, point-proton radius ( $r_p$ ), point-neutron radius ( $r_n$ ), point-nucleon-matter radius ( $r_m$ ), expectation values of  $\langle \mathbf{L} \cdot \mathbf{S} \rangle$  and  $\langle \mathbf{S}^2 \rangle$  for the neutron, and transition strengths ( $B(E2)$ , the neutron part ( $B(E2)_n$ ),  $B(IS2)$ , and  $B(IV2)$ ) for  $V_{LS} = 0-2000$  MeV.

$V_{LS}$ (MeV)	0	500	1000	1500	2000
BE ( $0_1^+$ ) (MeV)	-59.29	-59.54	-60.27	-61.43	-62.97
BE ( $2_1^+$ ) (MeV)	-57.14	-57.23	-57.57	-58.37	-59.78
BE ( $2_2^+$ ) (MeV)	-55.52	-55.79	-56.44	-57.14	-57.72
$r_p$ ( $0_1^+$ ) (fm)	2.548	2.535	2.498	2.448	2.393
$r_p$ ( $2_1^+$ ) (fm)	2.521	2.518	2.503	2.451	2.380
$r_p$ ( $2_2^+$ ) (fm)	2.546	2.526	2.489	2.476	2.474
$r_n$ ( $0_1^+$ ) (fm)	2.815	2.797	2.746	2.677	2.598
$r_n$ ( $2_1^+$ ) (fm)	2.791	2.787	2.765	2.693	2.597
$r_n$ ( $2_2^+$ ) (fm)	2.812	2.791	2.749	2.737	2.737
$r_m$ ( $0_1^+$ ) (fm)	2.712	2.695	2.650	2.588	2.518
$r_m$ ( $2_1^+$ ) (fm)	2.686	2.682	2.663	2.599	2.512
$r_m$ ( $2_2^+$ ) (fm)	2.709	2.688	2.648	2.636	2.635
$\langle \mathbf{L} \cdot \mathbf{S} \rangle$ ( $0_1^+$ )	-0.0002832	0.3766	0.6783	0.8871	1.025
$\langle \mathbf{L} \cdot \mathbf{S} \rangle$ ( $2_1^+$ )	-0.0007262	0.09012	0.2824	0.6649	0.9164
$\langle \mathbf{L} \cdot \mathbf{S} \rangle$ ( $2_2^+$ )	-0.002162	0.3583	0.4459	0.2394	0.1156
$\langle \mathbf{S}^2 \rangle$ ( $0_1^+$ )	0.001527	0.06294	0.2080	0.3717	0.5181
$\langle \mathbf{S}^2 \rangle$ ( $2_1^+$ )	0.002947	0.02264	0.1166	0.3520	0.5470
$\langle \mathbf{S}^2 \rangle$ ( $2_2^+$ )	0.002436	0.1035	0.2126	0.1503	0.09792
$B(E2: 2_1^+ \rightarrow 0_1^+)$ ( $e^2 \text{ fm}^4$ )	2.952	3.615	6.473	11.14	11.82
$B((E2)_n: 2_1^+ \rightarrow 0_1^+)$ ( $\text{fm}^4$ )	18.12	18.47	19.47	17.46	12.72
$B(IS2: 2_1^+ \rightarrow 0_1^+)$ ( $\text{fm}^4$ )	35.69	38.42	48.39	56.49	49.06
$B(IV2: 2_1^+ \rightarrow 0_1^+)$ ( $\text{fm}^4$ )	6.442	5.740	3.491	0.7058	0.01631
$B(E2: 2_2^+ \rightarrow 0_1^+)$ ( $e^2 \text{ fm}^4$ )	16.14	14.56	9.867	3.228	0.6455
$B((E2)_n: 2_2^+ \rightarrow 0_1^+)$ ( $\text{fm}^4$ )	5.861	4.443	1.108	0.4739	2.640
$B(IS2: 2_2^+ \rightarrow 0_1^+)$ ( $\text{fm}^4$ )	41.46	35.09	17.59	1.228	0.6747
$B(IV2: 2_2^+ \rightarrow 0_1^+)$ ( $\text{fm}^4$ )	2.549	2.917	4.363	6.175	5.897
$B(E2: 2_2^+ \rightarrow 2_1^+)$ ( $e^2 \text{ fm}^4$ )	12.75	15.30	22.45	15.92	4.390
$B((E2)_n: 2_2^+ \rightarrow 2_1^+)$ ( $\text{fm}^4$ )	0.5122	1.971	12.25	25.59	17.21
$B(IS2: 2_2^+ \rightarrow 2_1^+)$ ( $\text{fm}^4$ )	18.37	28.25	67.87	81.88	38.98
$B(IV2: 2_2^+ \rightarrow 2_1^+)$ ( $\text{fm}^4$ )	8.149	6.288	1.531	1.142	4.213

supports a triaxial  $\alpha + \alpha +$  dineutron clustering configuration. However, the  $B(E2: 2_2^+ \rightarrow 2_1^+)$  values with  $V_{LS} = 0$  and 500 MeV are smaller than that with 1000 MeV. This is considered to be caused by the further development of the dineutron cluster. Namely, the coupling pattern of the angular momentum among the two  $\alpha$  clusters and the dineutron cluster is different in the  $2_1^+$  and  $2_2^+$  states. Concretely, when the small  $V_{LS}$  value is adopted, it is considered that the two  $\alpha$  clusters with relative angular momentum  $L = 0$  are synthesized with the dineutron around them with  $L = 2$  in the  $2_1^+$  state. On the other hand, the two  $\alpha$  clusters with relative angular momentum  $L = 2$  are synthesized with the dineutron moving around them with  $L = 0$  in the  $2_2^+$  state. The decrease of the  $B(E2: 2_2^+ \rightarrow 2_1^+)$  value and the increase of the  $B(IV2: 2_2^+ \rightarrow 2_1^+)$  value corroborate the situation. We will discuss this situation again in Sects. 3.2 and 3.3.

Figure 1 shows the elastic cross section and inelastic cross section for the  $2_1^+$  state, and inelastic cross section for the  $2_2^+$  state of the  $^{10}\text{Be}$  nucleus obtained by the proton target at  $E/A = 59.4$  and 200 MeV. The two-dot-dashed, dot-dashed, dashed, dotted, and solid curves are obtained

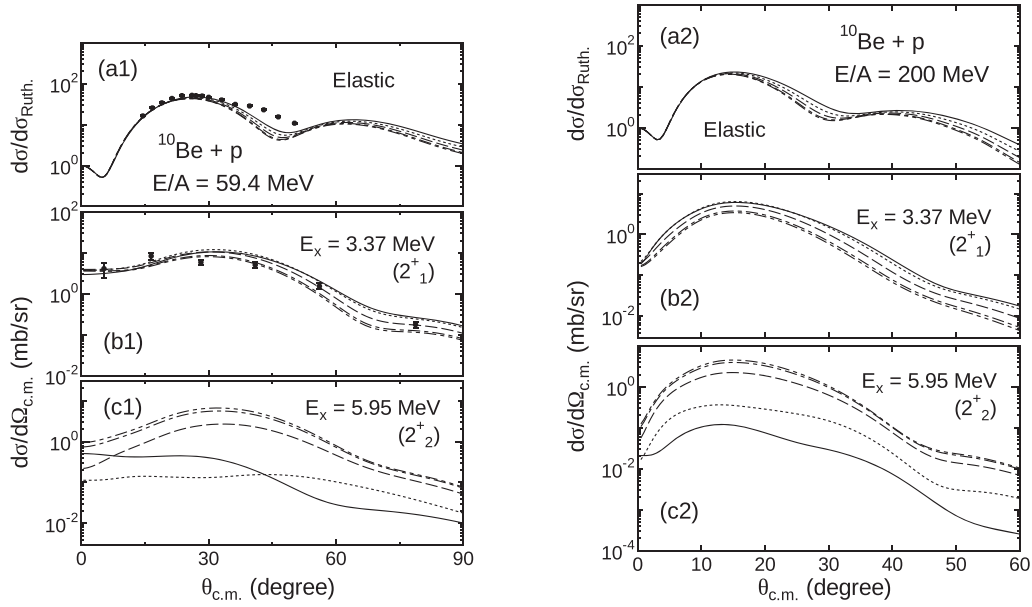


**Fig. 1.** (a1) Elastic cross section, (b1) inelastic cross section for the  $2_1^+$  state, and (c1) inelastic cross section for the  $2_2^+$  state of the  $^{10}\text{Be} + \text{p}$  system at  $E/A = 59.4$  MeV. (a2) Elastic cross section, (b2) inelastic cross section for the  $2_1^+$  state, and (c2) inelastic cross section for the  $2_2^+$  state of the  $^{10}\text{Be} + \text{p}$  system at  $E/A = 200$  MeV. The two-dot-dashed, dot-dashed, dashed, dotted, and solid curves are obtained with  $V_{\text{LS}} = 0, 500, 1000, 1500,$  and  $2000$  MeV, respectively. The experimental data are taken from Refs. [56–58].

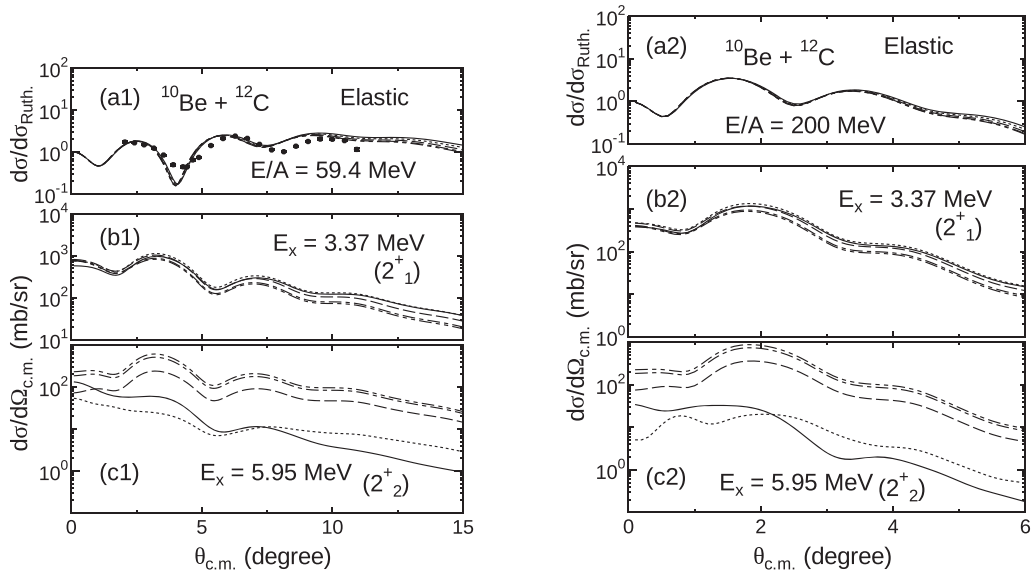


**Fig. 2.** Same as Fig. 1 but for the  $^{12}\text{C}$  target. The experimental data are taken from Refs. [56,57].

with  $V_{\text{LS}} = 0, 500, 1000, 1500,$  and  $2000$  MeV, respectively. The experimental data are well reproduced in a wide range of the  $V_{\text{LS}}$  values. We can see the drastic change of the inelastic cross sections for the  $2_2^+$  state depending on the  $V_{\text{LS}}$  value adopted in the structure calculation. This result has already been presented and discussed in Ref. [40]. However, we again show this result to compare with the additional calculation in this paper.

We also calculate the elastic and inelastic cross sections for the  $^{10}\text{Be} + ^{12}\text{C}$  system at  $E/A = 59.4$  and  $200$  MeV to investigate the effect of a different target. Figure 2 shows the elastic cross

**Table 2.** Same as Table 1 but for  $M = 0.52\text{--}0.64$ .

$M$	0.52	0.54	0.56	0.58	0.60	0.62	0.64
BE ( $0_1^+$ ) (MeV)	-77.07	-73.08	-69.39	-66.01	-62.97	-60.26	-57.90
BE ( $2_1^+$ ) (MeV)	-74.22	-70.17	-66.38	-62.91	-59.78	-57.05	-54.73
BE ( $2_2^+$ ) (MeV)	-69.52	-66.18	-63.11	-60.29	-57.72	-55.40	-53.34
$r_p$ ( $0_1^+$ ) (fm)	2.160	2.205	2.258	2.320	2.393	2.479	2.579
$r_p$ ( $2_1^+$ ) (fm)	2.139	2.180	2.231	2.296	2.380	2.488	2.617
$r_p$ ( $2_2^+$ ) (fm)	2.237	2.286	2.341	2.404	2.474	2.557	2.660
$r_n$ ( $0_1^+$ ) (fm)	2.298	2.357	2.426	2.506	2.598	2.702	2.816
$r_n$ ( $2_1^+$ ) (fm)	2.292	2.346	2.411	2.494	2.597	2.722	2.863
$r_n$ ( $2_2^+$ ) (fm)	2.446	2.509	2.579	2.655	2.737	2.828	2.933
$r_m$ ( $0_1^+$ ) (fm)	2.244	2.297	2.360	2.433	2.518	2.615	2.724
$r_m$ ( $2_1^+$ ) (fm)	2.232	2.281	2.341	2.416	2.512	2.631	2.767
$r_m$ ( $2_2^+$ ) (fm)	2.365	2.423	2.487	2.558	2.635	2.723	2.827
$\langle L \cdot S \rangle$ ( $0_1^+$ )	1.210	1.177	1.136	1.085	1.025	0.9571	0.8816
$\langle L \cdot S \rangle$ ( $2_1^+$ )	1.121	1.091	1.050	0.9938	0.9164	0.8123	0.6919
$\langle L \cdot S \rangle$ ( $2_2^+$ )	0.08979	0.08770	0.08810	0.1038	0.1156	0.1560	0.2073
$\langle S^2 \rangle$ ( $0_1^+$ )	0.7115	0.6723	0.6271	0.5755	0.5181	0.4560	0.3915
$\langle S^2 \rangle$ ( $2_1^+$ )	0.7017	0.6742	0.6416	0.6011	0.5470	0.4731	0.3835
$\langle S^2 \rangle$ ( $2_2^+$ )	0.1009	0.09268	0.08663	0.08654	0.09792	0.1241	0.1542
$B(E2: 2_1^+ \rightarrow 0_1^+)$ ( $e^2 \text{ fm}^4$ )	6.049	7.000	8.226	9.811	11.82	14.26	17.17
$B((E2)_n: 2_1^+ \rightarrow 0_1^+)$ ( $\text{fm}^4$ )	3.916	4.981	6.557	8.970	12.72	18.35	26.07
$B(\text{IS2}: 2_1^+ \rightarrow 0_1^+)$ ( $\text{fm}^4$ )	19.70	23.79	29.47	37.54	49.06	64.96	85.55
$B(\text{IV2}: 2_1^+ \rightarrow 0_1^+)$ ( $\text{fm}^4$ )	0.2309	0.1713	0.09447	0.01885	0.01631	0.2579	0.9271
$B(E2: 2_2^+ \rightarrow 0_1^+)$ ( $e^2 \text{ fm}^4$ )	0.02127	0.04007	0.09132	0.2363	0.6455	1.704	3.907
$B((E2)_n: 2_2^+ \rightarrow 0_1^+)$ ( $\text{fm}^4$ )	2.793	3.039	3.202	3.141	2.640	1.592	0.4369
$B(\text{IS2}: 2_2^+ \rightarrow 0_1^+)$ ( $\text{fm}^4$ )	2.327	2.382	2.212	1.654	0.6747	0.001903	1.731
$B(\text{IV2}: 2_2^+ \rightarrow 0_1^+)$ ( $\text{fm}^4$ )	3.302	3.777	4.375	5.100	5.897	6.589	6.958
$B(E2: 2_2^+ \rightarrow 2_1^+)$ ( $e^2 \text{ fm}^4$ )	0.09201	0.2346	0.6204	1.666	4.390	10.60	21.48
$B((E2)_n: 2_2^+ \rightarrow 2_1^+)$ ( $\text{fm}^4$ )	4.574	5.816	7.856	11.32	17.21	26.41	38.68
$B(\text{IS2}: 2_2^+ \rightarrow 2_1^+)$ ( $\text{fm}^4$ )	5.963	8.387	12.89	21.68	38.98	70.46	117.8
$B(\text{IV2}: 2_2^+ \rightarrow 2_1^+)$ ( $\text{fm}^4$ )	3.368	3.715	4.061	4.302	4.213	3.548	2.513

section, inelastic cross section for the  $2_1^+$  state, and inelastic cross section for the  $2_2^+$  state of the  $^{10}\text{Be} + ^{12}\text{C}$  system at  $E/A = 59.4$  and 200 MeV. The difference in the nuclear size has a minor effect on the elastic cross sections for the  $^{12}\text{C}$  target. The effect of Coulomb excitation on the inelastic cross section is minor. The inelastic cross sections for the  $2_1^+$  state for the  $^{12}\text{C}$  target have similar behavior to each other. Also, we can see the drastic change of the inelastic cross sections for the  $2_2^+$  state. Here, we note that the calculated inelastic cross sections for the  $2_2^+$  state show different behavior in comparison with the proton target for the solid and dotted curves. The results are caused by the weak IS transition strength shown in Table 1. In the present calculation for the  $^{12}\text{C}$  target, the IV component has no effect on the cross section. Comparing the proton target with  $^{12}\text{C}$ , the effect of the IS and IV components can be seen.

3.1.2. *Dependence on  $M$ .* Next, we investigate the dependence on the Majorana ( $M$ ) parameter. The  $M$  parameter is responsible for describing the  $NN$  exchange effect and is related to the Wigner ( $W$ ) parameter as  $W = 1 - M$ . Values of 0.56–0.63 are widely used in cluster model calculations. For the  $^{10}\text{Be}$  nucleus, 0.56 or 0.60 is usually adopted. Therefore, we investigate the range of  $M = 0.52\text{--}0.64$ , which is wider than the usual cases, in this paper.

Table 2 shows the calculated values of BEs, radii, expectation values, and quadrupole tran-



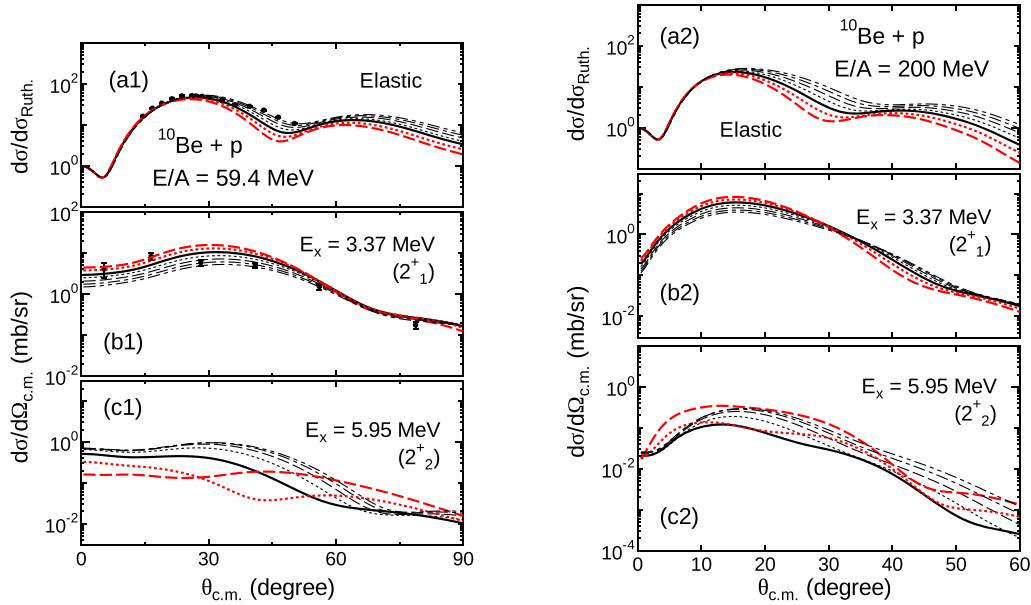


**Fig. 3.** Same as Fig. 1 but for  $M = 0.52$ – $0.64$ . The two-dot-dashed, dot-dashed, dashed, dotted, bold-solid, bold red dotted, and bold red dashed curves are obtained with  $M = 0.52, 0.54, 0.56, 0.58, 0.60, 0.62,$  and  $0.64$ , respectively.

sition strengths. Not only the  $V_{LS}$  parameter but also the  $M$  parameter give drastic changes in the BEs. With the increase of  $M$ , the repulsive effect becomes larger. Therefore, the large (small)  $M$  value gives weak (strong) binding. However, it is found that  $M$  has a minor effect on the excitation energy of the  $2_1^+$  state. On the contrary, when the  $M$  parameter is large, the difference of the energies between the  $2_1^+$  and  $2_2^+$  states becomes small. The sizes of the ground and excited states are also influenced by the change in the BE. Strong binding gives a small size for the ground and excited states. Therefore, the trend of the dependence of size on the  $M$  parameter is simple. Also, the expectation values show a simple increase or decrease, except for the  $\langle S^2 \rangle$  value of the  $2_2^+$  state, which shows minor dependence on the  $M$  value.

Next, we discuss the transition strength. Both of the proton and neutron parts of the transition strengths from the  $2_1^+$  state to the  $0_1^+$  state simply increase with the  $M$  parameter. The increase is concerned with the IS component. For the transition strength from the  $2_2^+$  state to the  $0_1^+$  state, the proton part increases, but the neutron part decreases with the  $M$  parameter. The increase of the proton part and the decrease of the neutron part give complicated transition strengths of the IS and IV components. The IV component of the transition strength from the  $2_2^+$  state to the  $0_1^+$  state is always larger than the IS component. This result is also different in comparison with the  $V_{LS}$  case. In addition, the transition strength from the  $2_2^+$  state to the  $2_1^+$  state gets larger with the  $M$  parameter. This indicates that we cannot ignore the multistep reaction effect on the inelastic cross section caused by the strong transition from the  $2_1^+$  state to the  $2_2^+$  state.

Figure 3 shows the elastic and inelastic cross sections calculated for the proton target with the experimental data. The two-dot-dashed, dot-dashed, dashed, dotted, bold-solid, bold red dotted, and bold red dashed curves are obtained with  $M = 0.52, 0.54, 0.56, 0.58, 0.60, 0.62,$  and  $0.64$ , respectively. The effect of changing the nuclear size is barely visible on the elastic cross section. We will discuss the effect of the BE, nuclear size, and elastic cross section again

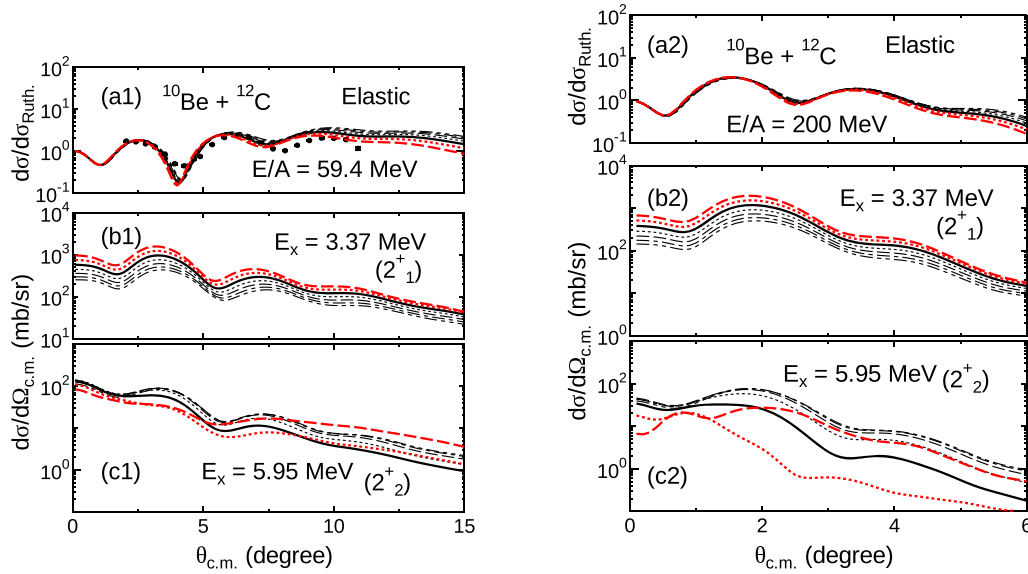


Fig. 4. Same as Fig. 3 but for the  $^{12}\text{C}$  target.

in Sect. 3.2. The effect of the change of the transition strength from the  $2_1^+$  state to the  $0_1^+$  state is barely visible on the inelastic cross section for the  $2_1^+$  state. On the contrary, we can see the drastic change of the inelastic cross sections for the  $2_2^+$  state. In Ref. [40], we expected that the change of the  $M$  parameter would not have much impact on the inelastic cross section. However, it indeed does give the change. Here, we compare the inelastic cross sections for the  $2_2^+$  state at  $E/A = 59.4$  with 200 MeV. At 59.4 MeV, the multistep reaction effect caused by the strong transition strength from the  $2_2^+$  state to the  $2_1^+$  state gives a complicated angular distribution. On the other hand, we can discuss the effect of changing the  $M$  parameter on the inelastic cross section for the  $2_2^+$  state at 200 MeV because the multistep reaction effect can be ignored at higher incident energy. The effect of changing  $M$  is indeed seen on the inelastic cross section for the  $2_2^+$  state at 200 MeV as shown in Fig. 3. Although this is smaller compared with the change of the  $V_{\text{LS}}$  parameter shown in Fig. 1, we cannot ignore the effect. Therefore, we will discuss the contribution of the  $V_{\text{LS}}$  and  $M$  parameters simultaneously in Sect. 3.2.

Figure 4 shows the elastic and inelastic cross sections calculated for the  $^{12}\text{C}$  target with the experimental data. Again, the change in the nuclear size has a minor effect on the elastic cross sections for the  $^{12}\text{C}$  target. The inelastic cross sections for the  $2_1^+$  state for the  $^{12}\text{C}$  target show similar behavior to that for the proton target. Also, we can see the drastic change of the inelastic cross sections for the  $2_2^+$  state. However, the behavior of the inelastic cross sections obtained with weak IS transition to the  $2_2^+$  state is slightly different in comparison with the proton target. This is caused by the small transition strength of the IS component. Again, we note that the IV component has no effect on the present calculation for the  $^{12}\text{C}$  target.

### 3.2. Effect of BE of the ground state

In the above subsections, we have only discussed the parameter dependence in nuclear structure calculations. That is, we did not specifically consider realistic physical points (e.g. BEs). In this subsection, we adjust the  $V_{\text{LS}}$  and  $M$  parameters so that the BEs of different parameter sets are reproduced consistent with each other as in Ref. [41]. In this paper, we first fix the  $V_{\text{LS}}$  value in the range of 0–2000 MeV and adjust the  $M$  parameter to obtain the appropriate BE. On the

**Table 3.** Same as Table 1 but for  $(V_{\text{LS}} \text{ (MeV)}, M) = (0, 0.57), (500, 0.57), (1000, 0.58), (1500, 0.59), \text{ and } (2000, 0.60)$ .

$V_{\text{LS}}$ (MeV)	0	500	1000	1500	2000
$M$	0.57	0.57	0.58	0.59	0.60
BE ( $0_1^+$ ) (MeV)	−62.79	−63.15	−62.79	−62.77	−62.97
BE ( $2_1^+$ ) (MeV)	−60.78	−60.90	−60.05	−59.72	−59.78
BE ( $2_2^+$ ) (MeV)	−59.27	−59.64	−59.04	−58.40	−57.72
$r_p$ ( $0_1^+$ ) (fm)	2.433	2.418	2.418	2.408	2.393
$r_p$ ( $2_1^+$ ) (fm)	2.410	2.407	2.419	2.402	2.380
$r_p$ ( $2_2^+$ ) (fm)	2.388	2.374	2.397	2.438	2.474
$r_n$ ( $0_1^+$ ) (fm)	2.681	2.660	2.651	2.628	2.598
$r_n$ ( $2_1^+$ ) (fm)	2.660	2.655	2.666	2.634	2.597
$r_n$ ( $2_2^+$ ) (fm)	2.639	2.621	2.645	2.695	2.737
$r_m$ ( $0_1^+$ ) (fm)	2.585	2.566	2.560	2.542	2.518
$r_m$ ( $2_1^+$ ) (fm)	2.563	2.559	2.570	2.544	2.512
$r_m$ ( $2_2^+$ ) (fm)	2.542	2.525	2.549	2.595	2.635
$\langle \mathbf{L} \cdot \mathbf{S} \rangle$ ( $0_1^+$ )	−0.00007341	0.4572	0.7533	0.9237	1.026
$\langle \mathbf{L} \cdot \mathbf{S} \rangle$ ( $2_1^+$ )	−0.0006060	0.1090	0.3788	0.7384	0.9164
$\langle \mathbf{L} \cdot \mathbf{S} \rangle$ ( $2_2^+$ )	−0.001788	0.4060	0.4069	0.1962	0.1156
$\langle \mathbf{S}^2 \rangle$ ( $0_1^+$ )	0.001095	0.08877	0.2521	0.4007	0.5181
$\langle \mathbf{S}^2 \rangle$ ( $2_1^+$ )	0.002028	0.02980	0.1667	0.3979	0.5470
$\langle \mathbf{S}^2 \rangle$ ( $2_2^+$ )	0.001607	0.1232	0.1971	0.1250	0.09792
$B(\text{E}2: 2_1^+ \rightarrow 0_1^+) (e^2 \text{ fm}^4)$	1.817	2.594	6.401	10.67	11.82
$B(\text{E}2)_n: 2_1^+ \rightarrow 0_1^+ (\text{fm}^4)$	13.53	13.95	16.05	14.83	12.72
$B(\text{IS}2: 2_1^+ \rightarrow 0_1^+) (\text{fm}^4)$	25.26	28.58	42.73	50.67	49.06
$B(\text{IV}2: 2_1^+ \rightarrow 0_1^+) (\text{fm}^4)$	5.429	4.514	2.181	0.3407	0.01631
$B(\text{E}2: 2_2^+ \rightarrow 0_1^+) (e^2 \text{ fm}^4)$	11.77	10.32	6.559	2.117	0.6455
$B(\text{E}2)_n: 2_2^+ \rightarrow 0_1^+ (\text{fm}^4)$	3.594	2.303	0.1438	1.022	2.640
$B(\text{IS}2: 2_2^+ \rightarrow 0_1^+) (\text{fm}^4)$	28.38	22.38	8.646	0.1970	0.6747
$B(\text{IV}2: 2_2^+ \rightarrow 0_1^+) (\text{fm}^4)$	2.358	2.874	4.760	6.081	5.897
$B(\text{E}2: 2_2^+ \rightarrow 2_1^+) (e^2 \text{ fm}^4)$	8.154	11.22	18.98	11.34	4.390
$B(\text{E}2)_n: 2_2^+ \rightarrow 2_1^+ (\text{fm}^4)$	0.002228	0.9923	13.58	22.47	17.21
$B(\text{IS}2: 2_2^+ \rightarrow 2_1^+) (\text{fm}^4)$	8.426	18.89	64.66	65.73	38.98
$B(\text{IV}2: 2_2^+ \rightarrow 2_1^+) (\text{fm}^4)$	7.886	5.539	0.4507	1.886	4.213

contrary, if the  $M$  parameter was first fixed in the range of 0.52–0.64, the appropriate  $V_{\text{LS}}$  value could not be obtained for the small  $M$  values of 0.52–0.56, when the constraint of reproducing the BE was imposed. The results are summarized in Table 3.

Table 3 shows the values of BEs, radii, expectation values, and quadrupole transition strengths calculated when using the  $V_{\text{LS}}$  and  $M$  values as parameters adjusting the BE of the ground state. The BEs of the ground state are obtained within a deviation of 1 MeV from the set of  $V_{\text{LS}} = 2000$  MeV and  $M = 0.60$ . The parameter set is also shown in Table 3. On the other hand, the excitation energies of the  $2_1^+$  and  $2_2^+$  states still depend on the set of the  $V_{\text{LS}}$  and  $M$  values. Here, we notice that the effect of the  $V_{\text{LS}}$  parameter is dominant for the excitation energy. By adjusting the BE of the ground state, the nuclear sizes of the ground state are obtained almost consistently. Namely, we can discuss other information without considering the effect of the size of the ground state, especially for the transition. The expectation values of  $\langle \mathbf{L} \cdot \mathbf{S} \rangle$  and  $\langle \mathbf{S}^2 \rangle$  are drastically dependent on the parameter set; they are strongly dependent

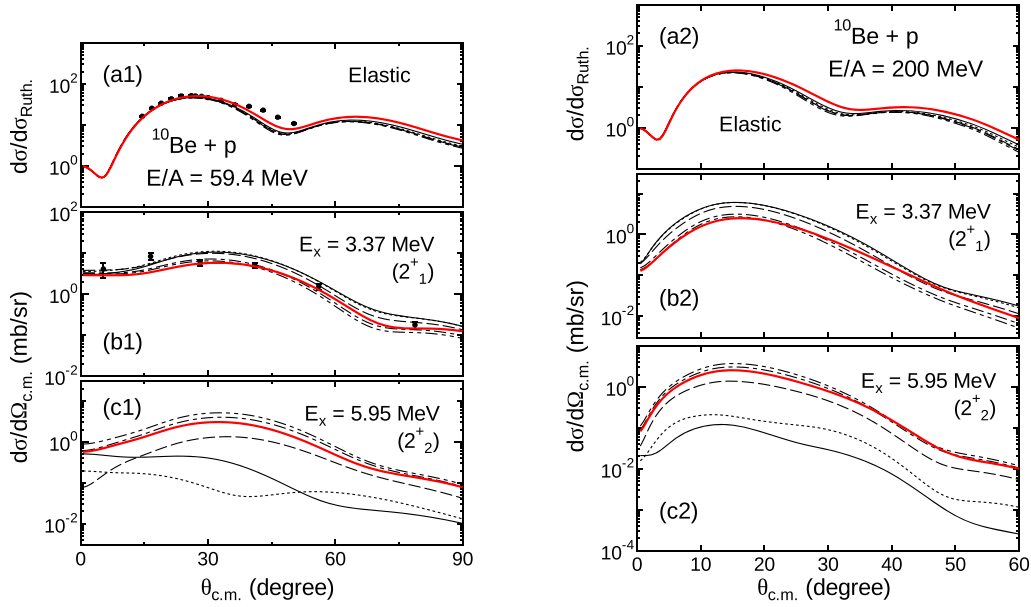


**Fig. 5.** Same as Fig. 1 but with the modification of  $M$ . The two-dot-dashed, dot-dashed, dashed, dotted, and solid curves are obtained with  $(V_{LS} \text{ (MeV)}, M) = (0, 0.57), (500, 0.57), (1000, 0.58), (1500, 0.59),$  and  $(2000, 0.60)$ , respectively. In addition, the bold red solid curve is the result obtained with the dineutron basis. The detail of the bold red solid curve is introduced in the next section.

on the  $V_{LS}$  parameter. Namely, the property of the  $^{10}\text{Be}$  nucleus strongly depends on the  $V_{LS}$  parameter even if we adjust the BEs of the ground state.

For the proton part of the transition strength from the  $2_1^+$  state to the  $0_1^+$  state, the difference of the  $V_{LS}$  and  $M$  values is not clearly seen. On the other hand, the neutron part shows that the change of the  $V_{LS}$  parameter has a significant effect. As a result, the IS and IV terms are strongly affected by the  $V_{LS}$  value for the transition from the  $2_1^+$  state to the  $0_1^+$  state. Also, the  $V_{LS}$  parameter has a dominant role to fix the transitions from the  $2_2^+$  state to the  $0_1^+$  state. Namely, the development and breaking of the dineutron correlation by the  $V_{LS}$  parameter appears through the transition from the  $2_2^+$  state to the  $0_1^+$  state as discussed in Sect. 3.1.1 and Ref. [40]. For the transition strength from the  $2_2^+$  state to the  $2_1^+$  state, the contribution of the  $V_{LS}$  parameter is dominant. Namely, the obtained nuclear structure information is strongly affected by the  $V_{LS}$  parameter even if the energies of the ground state are consistently reproduced by simultaneously changing the  $V_{LS}$  and  $M$  parameters.

Figure 5 shows the elastic and inelastic cross sections calculated for the proton target with the experimental data. The two-dot-dashed, dot-dashed, dashed, dotted, and solid curves are obtained with  $(V_{LS} \text{ (MeV)}, M) = (0, 0.57), (500, 0.57), (1000, 0.58), (1500, 0.59),$  and  $(2000, 0.60)$ , respectively. The meaning of the bold red solid curves will be explained in the next subsection. As mentioned before, adjusting the BE results in a similar nuclear size. We found that this gives similar elastic cross sections. The inelastic cross section for the  $2_1^+$  state is slightly affected by the set of  $V_{LS}$  and  $M$  parameters adopted. It is rather similar to results obtained by the  $V_{LS}$  parameter. On the other hand, a drastic change can be seen in the inelastic cross section for the  $2_2^+$  state. In addition, the results are similar to Fig. 1 which is obtained by changing only the  $V_{LS}$  parameter. Namely, the  $V_{LS}$  parameter has a dominant role for the inelastic cross section for both the  $2_1^+$  and  $2_2^+$  states even if the BE is adjusted by the  $V_{LS}$  and  $M$  parameters. In addition, the  $V_{LS}$  parameter has a role in the development and breaking of the dineutron correlation. If

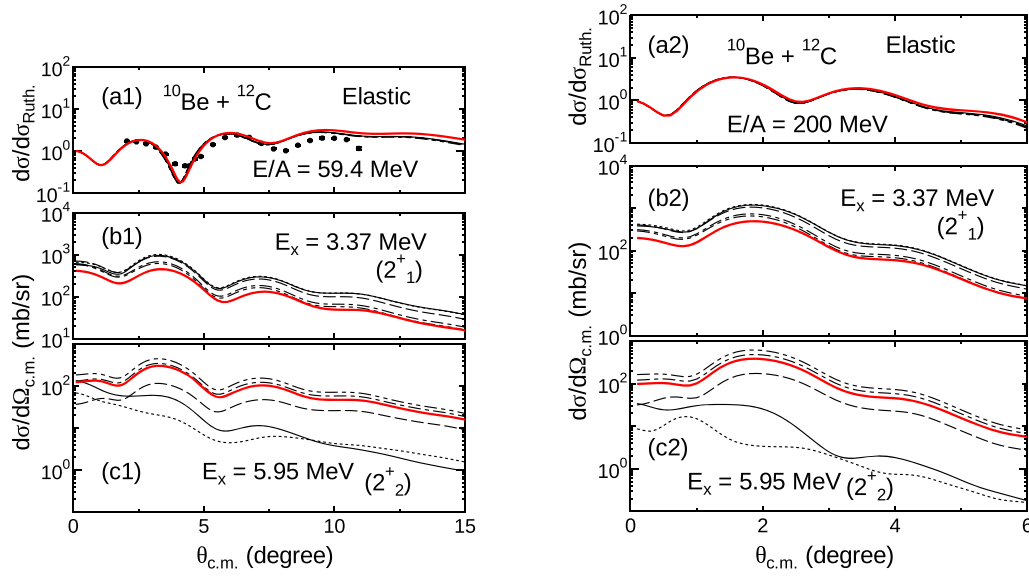


Fig. 6. Same as Fig. 5 but for the  $^{12}\text{C}$  target.

the  $V_{\text{LS}}$  value is small and the dineutron is well developed,  $K$ -mixing occurs and the inelastic cross section for the  $2_2^+$  is large. On the other hand, when the  $V_{\text{LS}}$  value is large and the dineutron structure is broken, no  $K$ -mixing occurs. Then, the inelastic cross section for the  $2_2^+$  state is small. However, we note that the inelastic cross section for the  $2_2^+$  state is slightly larger for larger spin orbitals such as 4000 MeV as shown in Ref. [40].

Figure 6 shows the elastic and inelastic cross sections calculated for the  $^{12}\text{C}$  target with the experimental data. Again, we can see the consistent results of the elastic cross sections owing to a similar nuclear size. In addition, we can see the drastic change of the inelastic cross section for the  $2_2^+$  state. These results are also similar to Fig. 2. Namely, the obtained results support the strong contribution of the  $V_{\text{LS}}$  parameter even if the energy of the ground state is consistently reproduced by varying the  $V_{\text{LS}}$  and  $M$  parameters simultaneously. Again, we see the effect of the IV term for the inelastic cross section for the  $2_2^+$  state in the comparison with the proton target.

### 3.3. Reconfirmation of behavior of inelastic cross section dependent on development and breaking of dineutron correlation

Next, we reconfirm the characteristic behavior of the inelastic cross section for the  $2_2^+$  state depending on the development and breaking of the dineutron correlation. We use the wave function constructed in the previous subsection and investigate the dineutron correlation in  $^{10}\text{Be}$ . To describe the dineutron correlation, we prepare the dineutron cluster as

$$\Psi_i = \mathcal{A}[\phi_\alpha(\mathbf{r}_{1-4}, \mathbf{R}_1)\phi_\alpha(\mathbf{r}_{5-8}, \mathbf{R}_2)\phi_{2n}(\mathbf{r}_{9-10}, \mathbf{R}_3)]_i, \quad (5)$$

where the positions of the centers of the wave packets for the two valence neutrons are the same. Here, the valence neutrons have spin up and down. Therefore, the dineutron cluster fully satisfies the condition of the dineutron correlation ( $S = 0$  and large spatial overlap). We fix the  $M$  parameter to be 0.54 to reproduce the BE of the ground state in the same manner as in the previous subsection.

With the dineutron cluster wave function, the obtained BEs are  $-63.46$ ,  $-61.33$ , and  $-60.40$  MeV for the  $0_1^+$ ,  $2_1^+$ , and  $2_2^+$  states, respectively. The calculated radii are 2.318, 2.289, 2.256,

2.445, 2.401, 2.386, 2.395, 2.357, and 2.335 fm for  $r_p(0_1^+)$ ,  $r_p(2_1^+)$ ,  $r_p(2_2^+)$ ,  $r_n(0_1^+)$ ,  $r_n(2_1^+)$ ,  $r_n(2_2^+)$ ,  $r_m(0_1^+)$ ,  $r_m(2_1^+)$ , and  $r_m(2_2^+)$ , respectively. The transition strengths are 1.677, 8.898, 18.30, 2.849, 7.940, 1.647, 16.82, 2.354, 7.434, 0.2712, 10.54, and 4.865 ( $e^2$ )fm<sup>4</sup> for  $B(E2: 2_1^+ \rightarrow 0_1^+)$ ,  $B((E2)_n: 2_1^+ \rightarrow 0_1^+)$ ,  $B(IS2: 2_1^+ \rightarrow 0_1^+)$ ,  $B(IV2: 2_1^+ \rightarrow 0_1^+)$ ,  $B(E2: 2_2^+ \rightarrow 0_1^+)$ ,  $B((E2)_n: 2_2^+ \rightarrow 0_1^+)$ ,  $B(IS2: 2_2^+ \rightarrow 0_1^+)$ ,  $B(IV2: 2_2^+ \rightarrow 0_1^+)$ ,  $B(E2: 2_2^+ \rightarrow 2_1^+)$ ,  $B((E2)_n: 2_2^+ \rightarrow 2_1^+)$ ,  $B(IS2: 2_2^+ \rightarrow 2_1^+)$ , and  $B(IV2: 2_2^+ \rightarrow 2_1^+)$ , respectively. The excitation energy is similar to the case with the weak  $V_{LS}$  parameter rather than the large one. The nuclear size obtained with the pure dineutron cluster is smaller than all other results in this paper. It is obvious that the expectation values of  $\langle \mathbf{L} \cdot \mathbf{S} \rangle$  and  $\langle \mathbf{S}^2 \rangle$  are zero. The transition strengths are also similar to the weak  $V_{LS}$  cases rather than the large one while the nuclear size is small. We note that the  $B(E2: 2_2^+ \rightarrow 2_1^+)$  value is smaller than the results obtained with  $V_{LS} = 0$ –1000 MeV shown in Table 1. This small  $B(E2: 2_2^+ \rightarrow 2_1^+)$  value implies the development of the  $\alpha + \alpha +$  dineutron cluster picture. Again, the coupling pattern of the angular momentum among the two  $\alpha$  clusters and the dineutron cluster is different in the  $2_1^+$  and  $2_2^+$  states. Concretely, when the small  $V_{LS}$  value is adopted, it is considered that the two  $\alpha$  clusters with relative angular momentum  $L = 0$  are synthesized with the dineutron around them with  $L = 2$  in the  $2_1^+$  state. On the other hand, the two  $\alpha$  clusters with relative angular momentum  $L = 2$  are synthesized with the dineutron moving around them with  $L = 0$  in the  $2_2^+$  state. The decrease of the  $B(E2: 2_2^+ \rightarrow 2_1^+)$  value and the increase of the  $B(IV2: 2_2^+ \rightarrow 2_1^+)$  value corroborate the situation. In addition, the result of the pure dineutron cluster implies that the developed dineutron cluster can be generated by employing the weak  $V_{LS}$  parameter.

Figures 5 and 6 show the results for the pure dineutron cluster state with the bold red solid curves. The effect of the nuclear size is not clearly seen on the elastic cross section. The results for the pure dineutron cluster state are consistent with those obtained with the weak  $V_{LS}$  value, especially for the inelastic cross section of the  $2_2^+$  state. Again, the development of the dineutron structure by the weak  $V_{LS}$  parameter is supported.

To confirm the development of the dineutron structure by the weak  $V_{LS}$  parameter, we calculate the component of the dineutron cluster, while this component is sensitive to basis states dependent on the random number. Here, we confirmed that the dependence of the basis states does not affect our conclusion. The component of the dineutron cluster for each state is listed in Table 4. Here the dineutron cluster component ( $C^{\text{dineutron}}(I_i^\pi)$ ) for the state  $\Phi(I_i^\pi)$  is defined as

$$C^{\text{dineutron}}(I_i^\pi) = \sum_k \langle \Phi(I_i^\pi) | \psi_k^{\text{dineutron}} \rangle \langle \psi_k^{\text{dineutron}} | \Phi(I_i^\pi) \rangle, \quad (6)$$

where  $\psi_k^{\text{dineutron}}$  is the  $k$ -th orthonormal state obtained by diagonalizing the Hamiltonian matrix only within the basis states of dineutron clusters introduced in Eq. (5). To clarify on which parameters the dineutron cluster component depends, we show in Table 4 not only the realistic cases but also cases where only the  $V_{LS}$  parameter or the  $M$  parameter is changed. The  $0_1^+$ ,  $2_1^+$ , and  $2_2^+$  states with the weak  $V_{LS}$  value have strong overlaps with the pure dineutron cluster state. With the increase of the  $V_{LS}$  value, the dineutron component becomes small. On the other hand, the components of dineutron configurations have a minor dependence on the  $M$  parameter for the  $0_1^+$  and  $2_1^+$  states. The dependence on the  $M$  parameter for the  $2_2^+$  state can be seen; however, the magnitude is smaller than the dependence on the  $V_{LS}$  parameter. This supports that the weak  $V_{LS}$  parameter gives the development of the dineutron cluster state in the  $^{10}\text{Be}$  nucleus.

**Table 4.** The components of dineutron configurations  $C^{\text{dineutron}}(I_i^\pi)$  defined in Eq. (6). The components are obtained with the wave functions constructed in Sects. 3.1.1, 3.1.2, and 3.2.

$V_{\text{LS}}$ (MeV)	0	500	1000	1500	2000		
		$M = 0.60$					
$C^{\text{dineutron}}(0_1^+)$	0.8516	0.8162	0.7562	0.6952	0.6424		
$C^{\text{dineutron}}(2_1^+)$	0.8125	0.7955	0.7555	0.6634	0.5763		
$C^{\text{dineutron}}(2_2^+)$	0.8345	0.7740	0.7074	0.7067	0.7129		
				$V_{\text{LS}} = 2000$ MeV			
$M$	0.52	0.54	0.56	0.58	0.60	0.62	0.64
$C^{\text{dineutron}}(0_1^+)$	0.5764	0.6003	0.6197	0.6338	0.6424	0.6465	0.6476
$C^{\text{dineutron}}(2_1^+)$	0.4951	0.5187	0.5401	0.5589	0.5763	0.5936	0.6095
$C^{\text{dineutron}}(2_2^+)$	0.7811	0.7761	0.7632	0.7421	0.7129	0.6777	0.6432
$V_{\text{LS}}$ (MeV)	0	500	1000	1500	2000		
$M$	0.57	0.57	0.58	0.59	0.60		
$C^{\text{dineutron}}(0_1^+)$	0.8794	0.8376	0.7603	0.6939	0.6424		
$C^{\text{dineutron}}(2_1^+)$	0.8524	0.8336	0.7628	0.6540	0.5763		
$C^{\text{dineutron}}(2_2^+)$	0.8762	0.8016	0.7316	0.7276	0.7129		

#### 4. Summary

We summarized the relationship between the nuclear structure and reaction within the  $^{10}\text{Be}$  nucleus by systematic analysis. The  $^{10}\text{Be}$  nucleus is constructed by changing the parameters of the effective  $NN$  interaction in the microscopic cluster model. The elastic and inelastic cross sections for proton and  $^{12}\text{C}$  targets at  $E/A = 59.4$  and 200 MeV were calculated with diagonal and transition densities obtained with various interaction parameters in the MCC calculation. The calculated elastic and inelastic cross sections well reproduce the experimental data.

In the construction of the  $^{10}\text{Be}$  nucleus, the strength of the spin-orbit potential ( $V_{\text{LS}}$ ) and the  $NN$  exchange effect ( $M$ ) are modified. The  $V_{\text{LS}}$  parameter has a strong effect on the nuclear structure. The BE, nuclear size, expectation value, and transition strength are drastically changed by the  $V_{\text{LS}}$  value. The elastic and inelastic cross sections are also dependent on the  $V_{\text{LS}}$  parameter. Especially, the value has an important role in the inelastic cross section of the  $2_2^+$  state. A difference in the IV component is slightly seen in the comparison of the proton and  $^{12}\text{C}$  targets. The  $M$  parameter also has an effect on the nuclear structure information. The calculated cross sections are also affected by this difference. The multistep reaction effect is also visible at  $E/A = 59.4$  MeV because the transition strength from the  $2_2^+$  state to the  $2_1^+$  state increases with the  $M$  parameter. On the other hand, we see a clear result without the multistep reaction effect at  $E/A = 200$  MeV. Comparing the results at 200 MeV, the effect of the  $V_{\text{LS}}$  parameter on the inelastic cross section of the  $2_2^+$  state is found to be larger than that of the  $M$  parameter. It is the  $V_{\text{LS}}$  parameter that changes the inelastic cross section of the  $2_2^+$  state most drastically. Since the degree of development of the dineutron correlation is highly dependent on the strength of the spin-orbit interaction, the structure of  $^{10}\text{Be}$  changes significantly and the cross section also changes with the  $V_{\text{LS}}$  parameter.

Next, we adjusted the  $V_{\text{LS}}$  and  $M$  parameters simultaneously to reproduce the BE of the ground state. We prepared different sets of these parameters and compared the obtained structure and the effect on the reaction. As a result, the property of the nuclear structure is found

to strongly depend on the  $V_{LS}$  parameter rather than the  $M$  parameter. The calculated cross sections are also dependent on the  $V_{LS}$  parameter. In addition, we prepared the pure dineutron cluster wave function to investigate the dineutron component in the  $^{10}\text{Be}$  nucleus by adjusting the  $V_{LS}$  and  $M$  parameters. It is found that the  $^{10}\text{Be}$  nucleus with the weak  $V_{LS}$  value has a large overlap with the pure dineutron cluster model. Therefore, we again conclude that the development and breaking of the dineutron correlation in  $^{10}\text{Be}$  are sensitive to changes in the spin-orbit contribution, thereby resulting in drastic changes in the inelastic scattering for the  $2_2^+$  state.

### Acknowledgements

This work was supported by Japan Society for the Promotion of Science (JSPS) KAKENHI Grant Numbers JP20K03944, JP21K03543, and JP22K03618. This work was supported by the collaborative research program at Hokkaido University.

### References

- [1] D. Vautherin and D.M. Brink, *Phys. Rev. C* **5**, 626 (1972).
- [2] J. Dechargé and D. Gogny, *Phys. Rev. C* **21**, 1568 (1980).
- [3] M. Kamimura, *Nucl. Phys.* **A351**, 456 (1981).
- [4] A. Ono, H. Horiuchi, T. Maruyama, and A. Ohnishi, *Prog. Theor. Phys.* **87**, 1185 (1992).
- [5] D. Baye, P. Descouvemont, and N.K. Timofeyuk, *Nucl. Phys.* **A577**, 624 (1994).
- [6] N. Itagaki, A. Ohnishi, and K. Katō, *Prog. Theor. Phys.* **94**, 1019 (1995).
- [7] P. Navrátil, J.P. Vary, and B.R. Barrett, *Phys. Rev. C* **62**, 054311 (2000).
- [8] T. Otsuka, R. Fujimoto, Y. Utsuno, B.A. Brown, M. Honma, and T. Mizusaki, *Phys. Rev. Lett.* **87**, 082502 (2001).
- [9] H. Nakada, *Phys. Rev. C* **68**, 014316 (2003).
- [10] T. Suhara and Y. Kanada-En'yo, *Phys. Rev. C* **82**, 044301 (2010).
- [11] M. Isaka and M. Kimura, *Phys. Rev. C* **92**, 044326 (2015).
- [12] A. Tohsaki, H. Horiuchi, P. Schuck, and G. Ropke, *Phys. Rev. Lett.* **87**, 192501 (2001).
- [13] Y. Kanada-Enyo, H. Horiuchi, and A. Ono, *Phys. Rev. C* **52**, 628 (1995).
- [14] T. Neff and H. Feldmeier, *Nucl. Phys. A* **738**, 357 (2004).
- [15] B. Sinha, *Phys. Rep.* **20**, 1 (1975).
- [16] F.A. Brieva and J.R. Rook, *Nucl. Phys.* **A291**, 299 (1977).
- [17] F.A. Brieva and J.R. Rook, *Nucl. Phys.* **A291**, 317 (1977).
- [18] F.A. Brieva and J.R. Rook, *Nucl. Phys.* **A297**, 206 (1978).
- [19] G.R. Satchler and W.G. Love, *Phys. Rep.* **55**, 184 (1979).
- [20] A.M. Kobos, B.A. Brown, P.E. Hodgson, G.R. Satchler, and A. Budzanowski, *Nucl. Phys.* **A384**, 65 (1982).
- [21] D.T. Khoa, W. von Oertzen, and H.G. Bohlen, *Phys. Rev. C* **49**, 1652 (1994).
- [22] L. Rikus and H.V.V. Geramb, *Nucl. Phys.* **A426**, 496 (1984).
- [23] D.T. Khoa, G.R. Satchler, and W. von Oertzen, *Phys. Rev. C* **56**, 954 (1997).
- [24] K. Amos, P.J. Dortmans, H.V. von Geramb, S. Karataglidis, and J. Raynal, *Adv. Nucl. Phys.* **25**, 275 (2000).
- [25] D.T. Khoa, *Phys. Rev. C* **63**, 034007 (2001).
- [26] T. Furumoto and Y. Sakuragi, *Phys. Rev. C* **74**, 034606 (2006).
- [27] D.T. Khoa, W. von Oertzen, H.G. Bohlen, and S. Ohkubo, *J. Phys. G: Nucl. Part. Phys.* **34**, R111 (2007).
- [28] T. Furumoto, Y. Sakuragi, and Y. Yamamoto, *Phys. Rev. C* **78**, 044610 (2008).
- [29] T. Furumoto, Y. Sakuragi, and Y. Yamamoto, *Phys. Rev. C* **80**, 044614 (2009).
- [30] T. Furumoto, Y. Sakuragi, and Y. Yamamoto, *Phys. Rev. C* **82**, 044612 (2010).
- [31] T. Furumoto, Y. Sakuragi, and Y. Yamamoto, *Phys. Rev. C* **94**, 044620 (2016).
- [32] Y. Sakuragi, M. Yahiro, and M. Kamimura, *Prog. Theor. Phys. Suppl.* **86**, 136 (1986).
- [33] M. Takashina, Y. Kanada-En'yo, and Y. Sakuragi, *Phys. Rev. C* **71**, 054602 (2005).
- [34] D.T. Khoa, D.C. Cuong, and Y. Kanada-En'yo, *Phys. Lett.* **B695**, 469 (2011).



- [35] W.W. Qu et al. Phys. Lett. **B751**, 1 (2015).
- [36] W.W. Qu et al. Phys. Rev. C **95**, 044616 (2017).
- [37] Y. Kanada-En'yo and K. Ogata, Phys. Rev. C **99**, 064601 (2019).
- [38] T. Furumoto and Y. Sakuragi, Phys. Rev. C **87**, 014618 (2013).
- [39] T. Furumoto, T. Suhara, and N. Itagaki, Phys. Rev. C **87**, 064320 (2013).
- [40] T. Furumoto, T. Suhara, and N. Itagaki, Phys. Rev. C **104**, 034613 (2021).
- [41] N. Itagaki, S. Hirose, T. Otsuka, S. Okabe, and K. Ikeda, Phys. Rev. C **65**, 044302 (2002).
- [42] T. Ichikawa, N. Itagaki, T. Kawabata, T. Kokalova, and W. von Oertzen, Phys. Rev. C **83**, 061301(R) (2011).
- [43] K. Muta, T. Furumoto, T. Ichikawa, and N. Itagaki, Phys. Rev. C **84**, 034305 (2011).
- [44] T. Furumoto, T. Suhara, and N. Itagaki, Phys. Rev. C **97**, 044602 (2018).
- [45] T. Furumoto and M. Takashina, Phys. Rev. C **103**, 044602 (2021).
- [46] A.B. Volkov, Nucl. Phys. **74**, 33 (1965).
- [47] K. Varga and J. Cseh, Phys. Rev. C **48**, 602 (1993).
- [48] M. Ito, K. Kato, and K. Ikeda, Phys. Lett. **B588**, 43 (2004).
- [49] Y. Kanada-En'yo, Phys. Rev. C **76**, 044323 (2007).
- [50] R. Tamagaki, Prog. Theor. Phys. **39**, 91 (1968).
- [51] N. Yamaguchi, T. Kasahara, S. Nagata, and Y. Akaishi, J. Phys. Soc. Jpn. **62**, 1018 (1979).
- [52] Y. Yamamoto, T. Furumoto, N. Yasutake, and T.A. Rijken, Phys. Rev. C **90**, 045805 (2014).
- [53] Y. Yamamoto, T. Furumoto, N. Yasutake, and T.A. Rijken, Eur. Phys. J **A52**, 19 (2016).
- [54] T. Furumoto, K. Tsubakihara, S. Ebata, and W. Horiuchi, Phys. Rev. C **99**, 034605 (2019).
- [55] D.T. Khoa, E. Khan, G. Colo, and N.V. Giai, Nucl. Phys. **A706**, 61 (2002).
- [56] <https://www.jcprg.org/exfor/>.
- [57] M.D. Cortina-Gil et al. Phys. Lett. **B401**, 9 (1997).
- [58] H. Iwasaki et al. Phys. Lett. **B481**, 7 (2000).